

Theory of probing a photonic crystal with transmission near-field optical microscopy

Garnett W. Bryant, Eric L. Shirley, and Lori S. Goldner

National Institute of Standards and Technology, Gaithersburg, Maryland 20899

Eric B. McDaniel and J. W. P. Hsu

Department of Physics, University of Virginia, Charlottesville, Virginia 22901

R. J. Tonucci

Naval Research Laboratory, Washington, D.C. 20375

(Received 20 January 1998)

While near-field scanning optical microscopy (NSOM) can provide optical images with resolution much better than the diffraction limit, analysis and interpretation of these images is often difficult. We present a theory of probing with transmission NSOM that includes the effects of tip field, tip/sample coupling, light propagation through the sample, and light collection. We apply this theory to analyze experimental NSOM images of a nanochannel glass (NCG) array obtained in transmission mode. The NCG is a triangular array of dielectric rods in a dielectric glass matrix with a two-dimensional photonic band structure. We determine the modes for the NCG photonic crystal and simulate the observed data. The calculations show large contrast at low numerical aperture (NA) of the collection optics and detailed structure at high NA consistent with the observed images. We present calculations as a function of NA to identify how the NCG photonic modes contribute to and determine the spatial structure in these images. Calculations are presented as a function of tip/sample position, sample index contrast and geometry, and aperture size to identify the factors that determine image formation with transmission NSOM in this experiment. [S0163-1829(98)06128-1]

I. INTRODUCTION

Near-field scanning optical microscopy (NSOM) is an exciting class of optical microscopies that can provide optical resolution much better than the diffraction limit.¹⁻⁶ One realization of NSOM uses an aperture that is much smaller than the wavelength λ of the light as a nearly pointlike (on the scale of λ) light source. Typically, an optical fiber is pulled to a 20–100-nm tip and metal coated, leaving a small hole in the metal coating at the tip to provide a nanometer-scale aperture. This aperture is then placed very close to the sample surface so that light emitted from the aperture does not diffract significantly before reaching the sample and superresolution, well below the diffraction limit $\lambda/2$, can be achieved. Components of the light that are strongly localized laterally by the aperture are evanescent, decaying rapidly as they move away from the aperture. Tip/sample distance can be adjusted to control the contribution from these evanescent tip fields.

NSOM images can now be readily obtained. A key step to the further development and application of NSOM is learning how to interpret, understand, and analyze these images. In NSOM, the excitation, the detection, or both can occur in the near field. Strong coupling between the sample and the light source/detector, which is not present in far-field optical microscopy, will occur in NSOM. For example, in transmission (reflection) NSOM, light from the metallized fiber tip couples to the sample in the near field of the tip, while the light transmitted (reflected) from the sample is collected in the far field. The NSOM images are influenced both by the strong sample/source coupling and by the far-field optics of

the collection process. To understand these images one must know how the localized source field is influenced by the presence of the sample in the near field, how light scatters from the sample, and how light is collected in the far field. In this paper, we present a theory for probing with transmission near-field optical microscopy. Our goal was to develop a theory capable of describing all parts of the imaging process. A complete theory is necessary to clearly identify and separate the contributions made by each step in the imaging process.

We apply this theory to understand transmission NSOM images⁷ made recently of a nanochannel-glass (NCG) array.⁸ These images probe the optical mode structure of this two-dimensional (2D) photonic crystal.⁹ The NCG array studied is a 2D triangular array of glass rods in a matrix made from a lower-index glass. By heating and pulling this structure the lattice constants of the array can be controlled. High-quality NCG's with lattice spacings on the order of or much less than λ can be made. The surfaces that are scanned have nearly flat topography. For these reasons, NCG's provide excellent samples for testing NSOM. A comparison between theory and experiment will identify which features of NSOM are important in this experiment, what determines the observed contrast and resolution in the transmission of NSOM images, and which features in the images depend on the details of the tip field.

The index variation of the NCG array is periodic in the 2D plane perpendicular to the glass rods, so the array possesses the optical modes of a 2D photonic crystal. Because the glass rods have the higher index, the distribution of these photonic modes in this 2D plane tends to be larger in the

glass rods. However, the index mismatch between core and matrix glasses is small for the sample studied, so significant coupling of these photonic modes among neighboring cores occurs as well. A comparison between theory and experiment will show what information about the 2D spatial distribution of the NCG photonic crystal modes can be learned from probing with transmission NSOM.

We briefly describe in Sec. II the experiment⁷ to be modeled and the key findings that we wish to understand. The theory used to model images obtained by transmission NSOM is presented in Sec. III. Each step in the process is modeled, including the tip fields, the optical modes of the sample, field propagation from the source through the sample to the detector, and collection of the transmitted light by the detector. The model used for the nanochannel glass array is also described in this section. In Sec. IV the calculations done to simulate the experiments are presented. The results show that the theory provides a good description of the observed images. The results allow us to determine which features of the near-field optics most affect these experiments. In this section we also present simulations for transmission NSOM of samples with much higher index contrast than that of the samples studied experimentally. Stronger coupling of the near field to the sample photonic modes is achieved by increasing the index contrast in the NCG. For this case we clearly identify those features in the transmission NSOM that arise from strong coupling of the source to the sample in the near field and determine how to enhance this coupling. Conclusions are presented in Sec. V.

II. EXPERIMENTAL RESULTS

The transmission NSOM experiment we model is shown schematically in Fig. 1. A metal coated fiber NSOM tip was placed about 10 nm from the sample surface. Light transmitted through the sample was collected in the far field by an objective with numerical aperture¹² (NA). The nanochannel glass-array sample was scanned in x and y at constant separation above the tip to produce a 2D image of the NCG. The images were taken with two different wavelengths of light ($\lambda = 670$ and 488 nm). Polarization of the light leaving the fiber tip was controlled by use of fiber paddles. Light was collected for three different NA's (NA = 0.28, 0.55, 0.7).

The nanochannel glass sample studied in the experiment⁷ was a 2D triangular lattice of one glass (channel glass) embedded in another glass (matrix glass) with similar but slightly lower index of refraction. The channel glass was cylindrical, approximately 745 nm in diameter with center-to-center nearest-neighbor separation of $1.07 \pm 0.05 \mu\text{m}$. The index of refraction of the matrix glass was 1.65–1.68 and that of the channel glass was 0.2–1.2 % higher in the visible range.

The detailed results for this experiment, including the gray-scale images made by transmission NSOM and line scans from these gray-scale images, are presented in Ref. 7. We summarize here the key findings. For low NA of the collection optics (NA = 0.28), the gray-scale images exhibit a triangular array of bright, circular spots with approximately 55% optical contrast between the bright regions, with maximum intensity I_b , and the dark regions, with minimum intensity I_d . The optical contrast is the change in intensity

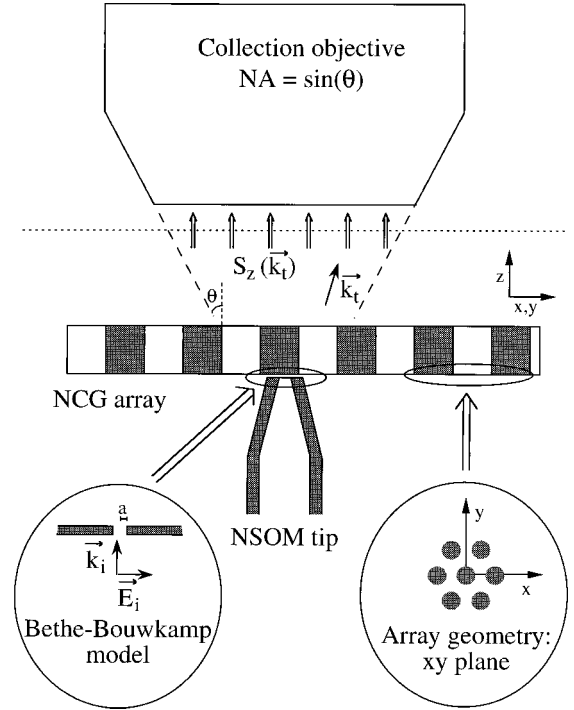


FIG. 1. Schematic of the transmission NSOM experiment. The nanochannel-glass array sample is scanned at constant separation across the NSOM tip. The transmitted light is collected by an objective with numerical aperture NA. Key elements of the theory are represented schematically. The tip field is described by the Bethe-Bouwkamp model (Refs. 10 and 11). The collected light is modeled as the total flux that leaves the sample inside the acceptance cone defined by NA and passes through a plane, as indicated, in the far field. The array geometry is indicated.

normalized by the average intensity $2(I_b - I_d)/(I_b + I_d)$. The center of a spot corresponds to the tip below the center of a channel-glass core. Similar results are seen for both λ . For intermediate NA (NA = 0.55), the images for the two λ are different. For the longer wavelength ($\lambda = 670$ nm), the bright spots flatten, the light to dark contrast is reduced to 38%, and the overall signal level increases. For the shorter wavelength ($\lambda = 488$ nm), the bright spots become rings, brightest when the tip is near but not at the channel glass edge, weaker when near the center of the channel glass core, and weakest outside the channel glass. The light to dark contrast is reduced to 25%. At the highest NA (NA = 0.70) this ring structure persists for the shorter wavelength with the contrast reduced to 15%. For the longer wavelength this ring structure begins to appear and the contrast ratio is reduced to 28%. These results are independent of the polarization of the tip field and weakly dependent on the aperture size and the tip/sample separation in the near field. Typical line scans are shown in Fig. 2 for NA = 0.70 with the tip about 10 nm from the sample. The scans were done along x , a direction that goes between two adjacent glass cores, as shown in Fig. 1. Diminished contrast and a weak contrast reversal are observed when the tip and sample are widely separated by approximately $1 \mu\text{m}$.

III. THEORY

To develop a complete theory for probing in transmission, we must have models for the incident tip field and for the

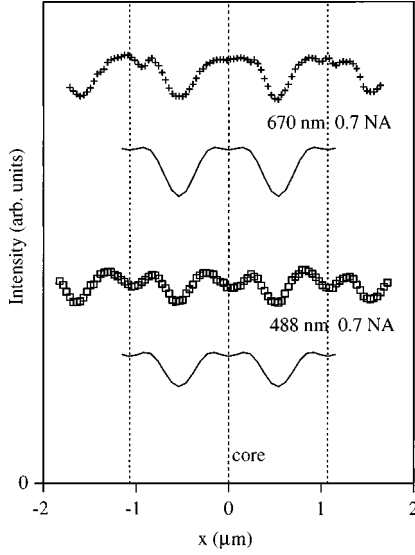


FIG. 2. Transmission as the tip scans along x : experimental scans ($\square, +$) and calculated scans ($—$) scaled to have the same average intensity and shifted for clarity. The core-glass centers are marked by vertical dashed lines. At $x=0$ the tip and core-glass centers are aligned.

electromagnetic modes of the sample. We must correctly account for the coupling of the incident field to the sample modes and for the coupling of the excited sample modes to reflected and transmitted fields. Finally, we must model the collection of the transmitted light. These steps are modeled in the following four sections.

A. Tip field

Rigorous, three-dimensional calculations of the fields emitted by a tip with a nanometer aperture are difficult and numerically intensive.^{6,13} The Bethe-Bouwkamp (BB) model^{10,11} is a simple approach that is commonly and successfully used^{13,14} instead of the numerically intensive approaches to model the tip field. In this paper, we use the BB model. As our results will show, the BB model provides an adequate representation for the tip fields in the experiments we describe so we did not test any of the models (see, for example, Refs. 15–17) that improve upon the BB model.

In the Bethe-Bouwkamp model, the near field of a tapered, metal-coated tip is modeled by the near field of the light transmitted by a circular aperture with radius a , in a perfectly conducting, thin, metal screen when a linearly polarized, plane-wave field is incident normal to the screen (see Fig. 1). Bethe and Bouwkamp calculated the fields, accurate to order $k_0 a$, $k_0 = 2\pi/\lambda$, for this problem 50 years ago.^{10,11} Most NSOM experiments are done in the range $0.1 < k_0 a < 1.5$, where the BB fields give reasonable results. As pointed out by Grober, Rutherford, and Harris, the higher-order corrections to the BB result change only the ratio of electric to magnetic field amplitudes without strongly affecting the spatial variation of the field.¹⁷

Bethe originally solved the problem in terms of a fictitious magnetic surface-charge density ρ_m and a magnetic surface-current density \mathbf{J}_m that exist inside the hole in the screen. Bouwkamp corrected the \mathbf{J}_m determined by Bethe. Magnetic vector and scalar potentials \mathbf{A}_m and ϕ_m were de-

termined from \mathbf{J}_m and ρ_m . The electric and magnetic fields transmitted by the aperture \mathbf{E}_{ap} and \mathbf{B}_{ap} , were obtained by taking appropriate derivatives of the vector and scalar potentials. Summarizing,

$$\mathbf{E}_{ap} = \nabla \times \mathbf{A}_m, \quad (1)$$

$$\mathbf{B}_{ap} = -ik_0 \mathbf{A}_m - \nabla \phi_m, \quad (2)$$

where

$$\mathbf{A}_m = - \int \mathbf{J}_m \frac{e^{ik_0 r}}{r} dA, \quad (3)$$

$$\phi_m = \int \rho_m \frac{e^{ik_0 r}}{r} dA. \quad (4)$$

The integrals are done over the area A of the aperture, and r is the distance from the field point to the source point in the aperture. For a plane-wave electric field, linearly polarized along x with amplitude E_0 and incident normal to the screen, the magnetic charge and current densities at a source point (x, y) inside the aperture are

$$\rho_m = - \frac{2yE_0}{\pi^2 \sqrt{a^2 - x^2 - y^2}} \quad (5)$$

and

$$J_{mx} = - \frac{2ik_0 xyE_0}{3\pi^2 \sqrt{a^2 - x^2 - y^2}}, \quad (6)$$

$$J_{my} = \frac{2ik_0 E_0 (2a^2 - x^2 - 2y^2)}{3\pi^2 \sqrt{a^2 - x^2 - y^2}}, \quad (7)$$

and

$$J_{mz} = 0. \quad (8)$$

The fields transmitted when the incident field is linearly polarized along y can be obtained from Eqs. (1)–(8) by applying the appropriate rotations. Transmitted fields for arbitrary incident polarization can be obtained from the appropriate linear combination of these two sets of fields.

All of the experimental images were made with the tip axis, taken here to be along the z direction as shown in Fig. 1, parallel to the glass rods in the NCG and normal to the NCG surface. To model images, we must do calculations for different positions of the aperture in an x - y plane at a fixed distance from the NCG and for different distances between the tip and the NCG surface. These calculations are most easily done in x - y Fourier space because the NCG is periodic in x and y . To do these calculations we need the 2D Fourier transform of the tip fields. We first obtain the 2D Fourier transform of the tip fields in an x - y plane a distance z_0 from the plane of the aperture, $\mathbf{E}_{ap}(k_x, k_y, z_0)$ and $\mathbf{B}_{ap}(k_x, k_y, z_0)$ by numerical fast-Fourier transform. From the

free-space propagation, we can obtain the Fourier transform of the tip field at any other x - y plane in free space at a distance z from the aperture. For the electric field,

$$\mathbf{E}_{\text{ap}}(k_x, k_y, z) = \exp[ik_z(z - z_0)] \mathbf{E}_{\text{ap}}(k_x, k_y, z_0), \quad (9)$$

where the wave vector k_z for propagation along z is obtained from the free-space dispersion of a mode with transverse wave vector (k_x, k_y) , $k_z = \sqrt{k_0^2 - k_x^2 - k_y^2}$. The phase of k_z is chosen so that the propagating modes (k_z real) are moving forward away from the aperture and the evanescent modes (k_z imaginary) are damped going away from the aperture. A similar equation applies for the magnetic field. Translations of the tip field in an x - y plane are achieved by translating the phase of the Fourier transform of the field. Shifting the tip from $(0, 0, z_{\text{ap}})$ to $(x_{\text{ap}}, y_{\text{ap}}, z_{\text{ap}})$ changes the Fourier components from $\mathbf{E}_{\text{ap}}(k_x, k_y, z_{\text{ap}})$ to $\exp[-i(k_x x_{\text{ap}} + k_y y_{\text{ap}})] \mathbf{E}_{\text{ap}}(k_x, k_y, z_{\text{ap}})$.

B. Optical modes of the nanochannel glass array

Typically, when the modes of a 2D photonic crystal are determined, the band structure for the mode frequency, ω vs k_x and k_y , is found for $k_z = 0$.⁹ To model transmission through an NCG, we need a different set of the optical modes; we need all propagating and evanescent modes, all k_z , for a given k_x , k_y , and ω . For that reason, we solve an eigenvalue problem for k_z rather than an eigenvalue problem for ω . We begin from the Maxwell equations for electric and magnetic fields \mathbf{E} and \mathbf{B} with frequency ω ,

$$\begin{aligned} \nabla \cdot \mathbf{B} &= 0, \\ \nabla \cdot n^2 \mathbf{E} &= 0, \\ \nabla \times \mathbf{B} &= -n^2 i \left(\frac{\omega}{c} \right) \mathbf{E}, \\ \nabla \times \mathbf{E} &= i \left(\frac{\omega}{c} \right) \mathbf{B}, \end{aligned} \quad (10)$$

where n is the local index of refraction in the NCG. Defining $\mathbf{F} = n\mathbf{E}$, then

$$\nabla \times \mathbf{E} = \nabla \times \left(\frac{1}{n} \mathbf{F} \right) = -\frac{\nabla n}{n^2} \times \mathbf{F} + \frac{1}{n} \nabla \times \mathbf{F}, \quad (11)$$

$$\nabla \cdot n^2 \mathbf{E} = \nabla \cdot n \mathbf{F} = n \nabla \cdot \mathbf{F} + \mathbf{F} \cdot \nabla n.$$

From this we have the following Maxwell equations:

$$\begin{aligned} \nabla \cdot \mathbf{B} &= 0, \\ \nabla \cdot \mathbf{F} + \mathbf{F} \cdot \frac{\nabla n}{n} &= 0, \\ \nabla \times \mathbf{B} &= -ni \left(\frac{\omega}{c} \right) \mathbf{F}, \\ \nabla \times \mathbf{F} - \frac{\nabla n}{n} \times \mathbf{F} &= ni \left(\frac{\omega}{c} \right) \mathbf{B}. \end{aligned} \quad (12)$$

Using the definition $\mathbf{g} = \nabla n/n$, the Maxwell equations become

$$\begin{aligned} \nabla \cdot \mathbf{B} &= 0, \\ \nabla \cdot \mathbf{F} + \mathbf{F} \cdot \mathbf{g} &= 0, \\ \nabla \times \mathbf{B} &= -ni \left(\frac{\omega}{c} \right) \mathbf{F}, \\ \nabla \times \mathbf{F} - \mathbf{g} \times \mathbf{F} &= ni \left(\frac{\omega}{c} \right) \mathbf{B}. \end{aligned} \quad (13)$$

To find the modes of the NCG, we treat the NCG as translationally invariant along z . The NCG is periodic in x and y , so n and \mathbf{g} have the form

$$n(x, y, z) = \sum_{\mathbf{G}} n(\mathbf{G}) \exp[i(G_x x + G_y y)], \quad (14)$$

$$\mathbf{g}(x, y, z) = \sum_{\mathbf{G}} \mathbf{g}(\mathbf{G}) \exp[i(G_x x + G_y y)].$$

The field modes must have the form

$$\begin{aligned} \mathbf{B}^{mq}(x, y, z) &= \sum_{\mathbf{G}} \mathbf{B}^{mq}(\mathbf{G}) \\ &\times \exp\{i[(q_x + G_x)x + (q_y + G_y)y + k_z^m z]\}, \end{aligned} \quad (15)$$

$$\begin{aligned} \mathbf{F}^{mq}(x, y, z) &= \sum_{\mathbf{G}} \mathbf{F}^{mq}(\mathbf{G}) \\ &\times \exp\{i[(q_x + G_x)x + (q_y + G_y)y + k_z^m z]\}, \end{aligned}$$

where \mathbf{G} are the 2D reciprocal lattice vectors for the NCG triangular lattice, \mathbf{q} is in the first Brillouin zone, and k_z^m is the eigenvalue for the m th mode for a given \mathbf{q} .

Define $k_x = q_x + G_x$, $k_y = q_y + G_y$ and the convolution $(n * F)(\mathbf{G}) = \sum_{\mathbf{G}'} n(\mathbf{G} - \mathbf{G}') F(\mathbf{G}')$ where the sum is over the 2D reciprocal lattice vectors \mathbf{G}' and similar definitions apply for other pairs of n or \mathbf{g} convolved with \mathbf{B} or \mathbf{F} . For a given \mathbf{q} , the Maxwell equations couple field-Fourier components with different \mathbf{G} . The equations are (suppressing the Fourier and eigenmode indices)

$$ik_x \mathbf{B}_y - ik_y \mathbf{B}_x + i \left(\frac{\omega}{c} \right) n * \mathbf{F}_z = 0, \quad (16)$$

$$ik_x \mathbf{F}_y - ik_y \mathbf{F}_x - g_x * \mathbf{F}_y + g_y * \mathbf{F}_x - i \left(\frac{\omega}{c} \right) n * \mathbf{B}_z = 0, \quad (17)$$

$$ik_x \mathbf{B}_x + ik_y \mathbf{B}_y + ik_z \mathbf{B}_z = 0, \quad (18)$$

$$ik_x \mathbf{F}_x + ik_y \mathbf{F}_y + ik_z \mathbf{F}_z + g_x * \mathbf{F}_x + g_y * \mathbf{F}_y = 0, \quad (19)$$

$$ik_y \mathbf{B}_z - ik_z \mathbf{B}_y = -i \left(\frac{\omega}{c} \right) n * \mathbf{F}_x, \quad (20)$$

$$ik_z \mathbf{B}_x - ik_x \mathbf{B}_z = -i \left(\frac{\omega}{c} \right) n * \mathbf{F}_y, \quad (21)$$

$$ik_y \mathbf{F}_z - ik_z \mathbf{F}_y - g_y * \mathbf{F}_z = i \left(\frac{\omega}{c} \right) n * \mathbf{B}_x, \quad (22)$$

$$ik_z \mathbf{F}_x - ik_x \mathbf{F}_z + g_x * \mathbf{F}_z = i \left(\frac{\omega}{c} \right) n * \mathbf{B}_y. \quad (23)$$

The first two equations, Eqs. (16) and (17), come from equations that have no derivatives of the z field components and have no dependence on k_z . These equations provide homogeneous constraints on the solutions to the eigenvalue problem defined by Eqs. (18)–(23). Written in explicit eigenvalue form, Eqs. (18)–(23) become

$$k_x \mathbf{B}_z - \left(\frac{\omega}{c} \right) n * \mathbf{F}_y = k_z \mathbf{B}_x, \quad (24)$$

$$k_y \mathbf{B}_z + \left(\frac{\omega}{c} \right) n * \mathbf{F}_x = k_z \mathbf{B}_y, \quad (25)$$

$$-k_x \mathbf{B}_x - k_y \mathbf{B}_y = k_z \mathbf{B}_z, \quad (26)$$

$$\left(\frac{\omega}{c} \right) n * \mathbf{B}_y + k_x \mathbf{F}_z + i g_x * \mathbf{F}_z = k_z \mathbf{F}_x, \quad (27)$$

$$-\left(\frac{\omega}{c} \right) n * \mathbf{B}_x + k_y \mathbf{F}_z + i g_y * \mathbf{F}_z = k_z \mathbf{F}_y, \quad (28)$$

$$-k_x \mathbf{F}_x + i g_x * \mathbf{F}_x - k_y \mathbf{F}_y + i g_y * \mathbf{F}_y = k_z \mathbf{F}_z. \quad (29)$$

Equations (24)–(29) and the two constraints, Eqs. (16) and (17), guarantee that for a given \mathbf{q} we will have four modes per \mathbf{G} . These four modes correspond to two polarizations for each k_z and $-k_z$. For $k_z \rightarrow -k_z$, we have $(\mathbf{F}_x, \mathbf{F}_y, \mathbf{F}_z) \rightarrow (-\mathbf{F}_x, -\mathbf{F}_y, \mathbf{F}_z)$ and $(\mathbf{B}_x, \mathbf{B}_y, \mathbf{B}_z) \rightarrow (\mathbf{B}_x, \mathbf{B}_y, -\mathbf{B}_z)$, as can be checked by inspection of Eqs. (16), (17), and (24)–(29).

C. Field transmission

We determine the transmission of the incident tip field through the NCG by solving the standard boundary matching problem for transmission through a film. We assume that the total field in the free-space region containing the tip is the incident tip-field plus the field reflected by the NCG. Explicitly, the reflected field is

$$\mathbf{E}_r(x, y, z) = \sum_{\mathbf{k}, p} \mathbf{E}_{r,p}(\mathbf{k}) \exp[i(k_x x + k_y y + k_z^r z)], \quad (30)$$

where the sum is over lateral wave vectors $\mathbf{k} = (k_x, k_y)$ and the two polarizations p . The z wave vector k_z^r is obtained from the free-space dispersion $k_z^r = \sqrt{k_0^2 - k_x^2 - k_y^2}$. The phase of k_z^r is chosen so that propagating modes are forward propagating and evanescent modes are damped as the mode moves from the NCG sample back toward the tip. The two polarization vectors $\mathbf{E}_{r,p}(\mathbf{k})$ are chosen to ensure that $\nabla \cdot \mathbf{E} = 0$ for each free-space mode. Reflections off the tip are not included. This is the only approximation, other than the use of the Bethe-Bouwkamp model for the source field, that we make for the local fields near the tip. As our results will show, including multiple reflections is not important for the experiments we model. \mathbf{B}_r is defined by a similar

equation. The field in the free-space region containing the collection optics is the transmitted field,

$$\mathbf{E}_t(x, y, z) = \sum_{\mathbf{k}, p} \mathbf{E}_{t,p}(\mathbf{k}) \exp[i(k_x x + k_y y + k_z^t z)], \quad (31)$$

where k_z^t is determined from the free-space dispersion. The phase of k_z^t is chosen so that propagating modes are forward propagating and evanescent modes are damped as the mode moves from the NCG sample toward the collector. The field in the NCG is

$$\mathbf{E}_{\text{NCG}}(x, y, z) = \sum_{m, \mathbf{q}} \alpha_{m\mathbf{q}} \mathbf{E}^{m\mathbf{q}}(x, y, z), \quad (32)$$

where the $\alpha_{m\mathbf{q}}$ are the amplitudes for the modes excited in the NCG. At each NCG surface, we have the boundary conditions that the two tangential electric field components E_x and E_y and the two tangential magnetic field components B_x and B_y be continuous. These four conditions define the set of matrix equations that are solved to determine the amplitudes for the Fourier components of the reflected and transmitted fields and for the excited NCG modes.

When calculating transmission through a film, one must worry about the effects of multiple reflections between the sample surfaces that can produce resonant transmission and Fabry-Pérot oscillations. We calculate transmission for thick NCG samples, as used in the experiments. These samples are much thicker than λ . We also do calculations for films much thinner than λ . We study these two limits to investigate the effect of sample thickness on image formation. We have no problem doing the calculations when the film is thinner than λ , because transmission resonances do not occur. For the thick samples, we have to be more careful. Resonances can be sharp when the sample has a uniform thickness that is much greater than λ . In real samples these resonances are broadened because the sample thickness is not uniform. However, our calculations are done for samples with uniform thickness. Spurious effects from sharp resonances in the transmission can occur because we include only a finite set of reciprocal lattice vectors in our representations of the index and the fields [Eqs. (14) and (15)]. Typically, we sum over all reciprocal lattice vectors with lengths less than 3–4 times the length of the fundamental reciprocal lattice vectors. Numerical diagonalization to find the eigenmodes becomes very time consuming if we include more reciprocal lattice vectors. Small changes in the cutoffs make only small changes in the modes. This can result in large changes of the specific modes that are resonant at a particular sample thickness. We have checked that the effects of these resonances are spurious by varying cutoffs for the wave vectors we include and by varying the sample thickness. We can eliminate these spurious effects by increasing the cutoffs. However, for typical cases, it is computationally too expensive to increase the cutoff enough to eliminate all spurious effects. To eliminate these spurious effects simply, we add a damping factor to all of the propagating NCG modes. For all NCG modes with real k_z , we include an imaginary term [typically $0.01 \mu\text{m}^{-1}$] to the z wave vector to damp waves as they propagate across the sample. This damping reduces the effects of the multiple reflections between the sample surfaces, broadens the resonances, and thereby eliminates the spurious

effects in the contribution from resonances. In the experiments, variations in sample thickness break the coherence of multiple reflections and eliminate resonance effects. Our use of a damping factor is a simple way to mimic this phase breaking and eliminate resonance effects. We use the same damping for all propagating waves. We also choose this damping to be much weaker than the damping of any of the evanescent modes. As a consequence, the damping we introduce reduces the overall intensity of the transmitted light without affecting the relative transmission amplitudes of different Fourier components of the transmitted light. Thus, the damping that we include does not affect the transmission line scans we calculate, other than to change the absolute scale of the transmission intensities. We get the same transmission line scans, except for the overall scale factor, when we eliminate spurious effects of the resonances by increasing the wave-vector cutoff.

D. Image formation

To model transmission-NSOM images, we need to calculate the amount of the transmitted light that is collected by optics with a numerical aperture NA. We use the following simple model (see Fig. 1). We assume that the optics collects all of the transmitted flux that passes through an x - y plane in the far field away from the NCG. All flux leaving the NCG within the numerical aperture of the optics, the angle θ in Fig. 1, is collected.

To calculate the total intensity of the collected light I we first need the time-averaged Poynting vector for a harmonic free-space field with frequency ω ,

$$\langle \mathbf{S}(x, y, z) \rangle = \frac{c}{8\pi} \text{Re}\{\mathbf{E}(x, y, z) \times \mathbf{B}^*(x, y, z)\}. \quad (33)$$

The flux passing through an x - y plane in the far field is $\langle S_z(x, y, z \rightarrow \infty) \rangle$.

Using a 2D Fourier expansion to write the fields,

$$\mathbf{E}(x, y, z) = \sum_{k_x, k_y} \mathbf{E}(k_x, k_y) \exp[i(k_x x + k_y y)] \exp[ik_z(z - z_s)], \quad (34)$$

where z_s is the position of the back sample surface, the sum is over all 2D k space, k_z is obtained from the free-space dispersion, and the phase of k_z is chosen to give forward-propagating or damped waves going into free space away from z_s . A similar equation holds for \mathbf{B} . The integrated flux passing through the x - y plane at z is the total intensity,

$$\begin{aligned} I_{\text{tot}} &\equiv \frac{1}{(2\pi)^2} \int dx dy \langle S_z(x, y, z) \rangle \\ &= \frac{c}{8\pi} \text{Re} \left\{ \sum_{k_x, k_y} \hat{\mathbf{z}} \cdot [\mathbf{E}(k_x, k_y) \times \mathbf{B}^*(k_x, k_y)] \right. \\ &\quad \left. \times \exp[i(k_z - k_z^*)(z - z_s)] \right\}. \end{aligned} \quad (35)$$

For propagating modes $k_z = k_z^*$ and for evanescent modes $k_z = -k_z^*$. In the far-field limit, the exponential factor vanishes for evanescent modes and is 1 for propagating modes, thus

$$\begin{aligned} I_{\text{tot}} &= \frac{c}{8\pi} \sum_{\sqrt{k_x^2 + k_y^2} \leq 2\pi/\lambda} \text{Re}\{E_x(k_x, k_y)B_y^*(k_x, k_y) \\ &\quad - E_y(k_x, k_y)B_x^*(k_x, k_y)\}. \end{aligned} \quad (36)$$

The optics collects light within the cone defined by the numerical aperture, reducing the cutoff for light collection from the free-space cutoff $2\pi/\lambda$ to $2\pi\text{NA}/\lambda$ where $\text{NA} = \sin \theta$ in free space. Thus, the total intensity of transmitted light I collected by the optics is

$$\begin{aligned} I &= \frac{c}{8\pi} \sum_{\sqrt{k_x^2 + k_y^2} \leq 2\pi\text{NA}/\lambda} \text{Re}\{E_x(k_x, k_y)B_y^*(k_x, k_y) \\ &\quad - E_y(k_x, k_y)B_x^*(k_x, k_y)\}. \end{aligned} \quad (37)$$

Simulated images are obtained by calculating I as a function of the relative positions of the tip and sample. In this paper we present one-dimensional line scans of these images.

E. Nanochannel glass model

As shown in Fig. 1, the NCG sample is a 2D triangular lattice of glass rods in a glass matrix. We assume that rods are perfect cylinders. In the experiments, the lattice spacing is $1.07 \mu\text{m}$ and the core radius $r_c = 0.37 \mu\text{m}$. We use these values to model the measured images. We do additional calculations with other lattice parameters to further test the potential of NSOM for probing these structures. The measured samples are approximately $250 \mu\text{m}$ thick. We use this thickness to model the measured images. Our results for thick samples are insensitive to sample thickness because we eliminate Fabry-Pérot oscillations by use of the damping factor. We also consider thin samples where sample evanescent modes, excited by the tip field, can be transmitted through the sample. We assume that the index of refraction is real and uniform in each glass, has the bulk value in each glass, and has a step discontinuity at the core/matrix glass interface. This is the only assumption that we make about the dielectric structure of the NCG. The matrix glass has a bulk index of refraction of 1.678 for $\lambda = 488 \text{ nm}$ and 1.657 for $\lambda = 670 \text{ nm}$.⁷ The core glass has a higher index so it acts as a guiding region. For $\lambda = 488 \text{ nm}$, the index difference is $\Delta n \approx 0.011$.⁷ For $\lambda = 670 \text{ nm}$, the index difference is $\Delta n \approx 0.019$.⁷ We use these values to model the measured images. Other calculations are done with higher Δn for additional tests. The scanned NCG surface was polished. The core glass etches preferentially during polishing, leaving $3.5 \pm 0.5 \text{ nm}$ depressions centered on the channel glasses. The experimental scans are done at constant separation z_{ap} between the tip aperture and the NCG. For the calculations, we model a flat surface, ignoring the effect of these small depressions on the fields at the sample surface. Our results show that the transmission NSOM images are determined by the coupling of the tip fields to the *bulk* photonic modes of the NCG and should not depend on the surface structure. Also, our results do not change much for nm-scale changes in z_{ap} or sample thickness so we can ignore topographic effects on the calculated images.

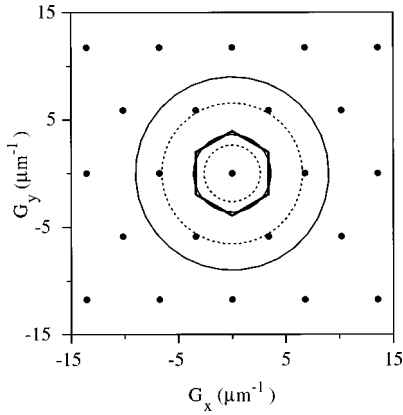


FIG. 3. Reciprocal lattice points (●) and first Brillouin zone boundary (—) for the NCG sample. Cutoff wave vectors for $\lambda = 488$ nm (—) and 670 nm ($\cdot \cdot \cdot$) are shown. Each inner (outer) circle is for $\text{NA} = 0.28$ (0.7).

F. Significance of NA and k -space cutoffs

Our NCG experiments,⁷ as well as other experiments,¹⁸ show that collection optics NA has a strong effect on transmission NSOM image contrast. The collection optics NA determines which transmitted modes are collected. Figure 3 shows the reciprocal-lattice points for the sample studied experimentally. Also shown are the boundary for the first Brillouin zone and the cutoffs for the transverse wave vector that determine which transmitted modes are collected by the optics for different λ and NA [see Eq. (37)]. The transverse wave vectors for transmitted modes that are collected by the optics lie inside the cutoff. As NA increases, the cutoff for mode components that are collected by the far-field detector increases. Also, for fixed NA the cutoff increases with decreasing λ . For $\text{NA} = 0.28$, the cutoffs lie well inside (at) the boundary of the first Brillouin zone for $\lambda = 670$ nm (488 nm). For $\text{NA} = 0.7$, the cutoff extends to the edge of the second Brillouin zone for $\lambda = 670$ nm and into the fourth Brillouin zone for $\lambda = 488$ nm. From our results we find that the scans for different λ are similar if the scans have similar cutoffs and thus have contributions from similar sets of transverse wave vectors. Thus the scans for $\lambda = 670$ nm are similar to those scans for $\lambda = 488$ nm done at smaller NA.

IV. RESULTS

A. Line scans

First, we show that the theory is able to describe the images of the NCG made with transmission NSOM. Calculated line scans along x of the transmitted intensity are shown in Figs. 4 and 5 for $\lambda = 488$ and 670 nm, respectively. The intensities are given in arbitrary units. However, the same units are used for these two figures and for all other figures that deal with the same NCG, except where it is noted that the results have been rescaled. Thus, intensities plotted in different figures for the same NCG can usually be compared directly. The dependence on NA is shown. The calculated line scans reproduce the key features in the measured line scans. For small NA, the line scans are peaked at the channel glass centers, with a peak/valley intensity ratio of about 1.5, even though the index contrast is only 1–2 %. As NA in-

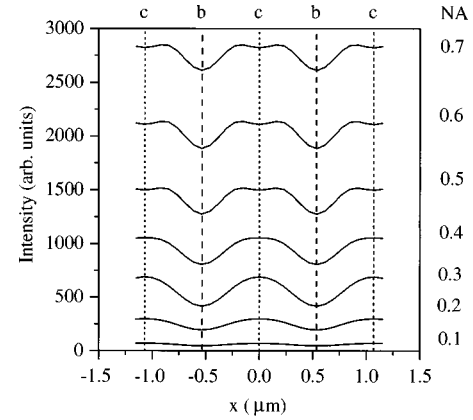


FIG. 4. Transmitted intensity line scan along x : $\lambda = 488$ nm, tip/sample separation $z_{\text{ap}} = 10$ nm, tip radius $a = 50$ nm. Dependence on collection optics NA is shown. Positions of channel-glass centers (c) and bridge sites (b), the midpoints on the lines joining adjacent glass centers, are shown.

creases, more of the transmitted light is collected and the average transmitted intensity increases. The peaks broaden and flatten and the peak/valley ratio decreases. At $\text{NA} = 0.5$ (0.7) for $\lambda = 488$ (670) nm, the peaks about core centers develop structure with depressions in the middle and side peaks $\approx 0.2 \mu\text{m}$ from the centers. These side peaks produce the ring structure observed in the experimental images. The experimental images at 0.7NA show the rings prominently for $\lambda = 488$ nm but only hint that rings are starting to appear for $\lambda = 670$ nm. Our calculations also show that the rings form at lower NA for shorter λ . This occurs because more of k space is collected, for a given NA, for shorter λ . Scans along other directions (see Fig. 6 for scans along y) give similar results. In particular, the structure inside the glass core is identical for the scans along different directions, confirming the cylindrical symmetry of this structure. This gives evidence that the structure in the peak is due to transmitted light that propagates through the sample in photonic modes that are concentrated in the cylindrically symmetric cores.

Figure 2 shows a comparison of the experimental and calculated line scans along x at $\text{NA} = 0.7$ for both λ . The curves have been scaled to have the same average value and then shifted for clarity. There is strong qualitative agreement

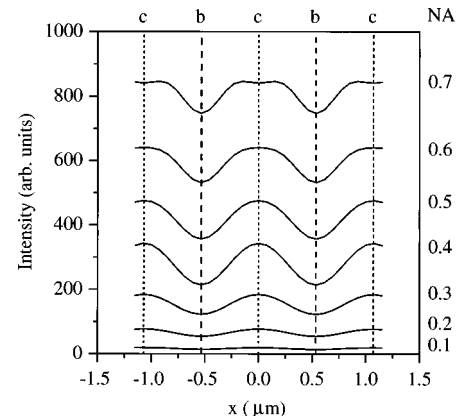


FIG. 5. Transmitted intensity line scan along x : $\lambda = 670$ nm, $z_{\text{ap}} = 10$ nm, $a = 50$ nm. Dependence on NA is shown. Positions of channel-glass centers (c) and bridge sites (b) are shown.

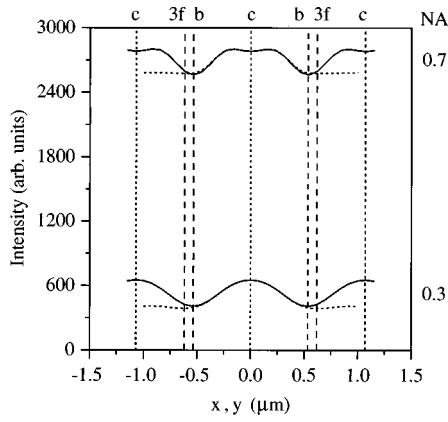


FIG. 6. Comparison of transmitted intensity line scans along x (—) and y (· · · ·): $\lambda = 488$ nm, $z_{\text{ap}} = 10$ nm, $a = 50$ nm. Positions of channel-glass centers (c), bridge sites (b) along x , and threefold sites (3f) along y are shown. The threefold symmetric sites are at the middle of the triangles formed by three adjacent nearest-neighbor glass centers.

between the data and the calculations, as we have already discussed. The ring structure occurs at similar positions, well inside the edge of the channel glass, in both the experimental and calculated scans. This ring structure is not directly related to the channel glass edge but is connected to the spatial distribution of NCG photonic modes. The most noticeable differences are in the intensity ratios. The depressions in the peaks for 488 nm are more pronounced in the experimental line scans than in the calculated scans. The experimental data typically show more contrast than the calculations. For example, the small dip in intensity at the threefold site for a y scan is harder to see in the calculated scans (see Fig. 6) than in the experimental data.⁷ The experimental intensity ratios at 0.28 NA, for peak/threefold site and bridge/threefold site are 1.58 and 1.18 for $\lambda = 488$ nm and 1.60 and 1.10 for $\lambda = 670$ nm.⁷ The calculated ratios at 0.3NA are 1.69 and 1.05 for $\lambda = 488$ nm and 1.51 and 1.02 for $\lambda = 670$ nm. At 0.7NA, the experimental peak/threefold site intensity ratios are 1.15 for $\lambda = 488$ nm and 1.28 for $\lambda = 670$ nm.⁷ The calculated ratios at 0.7NA are 1.08 for $\lambda = 488$ nm and 1.14 for $\lambda = 670$ nm. In all cases, the experimental and calculated intensity ratios are similar. In all cases except one, the experimental ratio is larger than the calculated ratio. This suggests that the calculations may underestimate slightly the coupling to the NCG modes that are concentrated in the glass cores and produce the structure in the line scans. Some of the small disagreement between experimental and calculated intensity ratios can probably be removed by using better models for the NCG and its dielectric profile, the tip field, or the multiple scattering between the tip and the NCG. We have not yet tested these possibilities.

Consider the following *simple* analysis of the transmitted intensity to understand the structure in the line scans. The index difference between the core and matrix glasses in the NCG is small, so much of the collected light will be transmitted through the NCG in extended, nearly uniformly distributed modes. The channel glass does have the higher index, so some of the collected light will be transmitted in modes more concentrated in the glass cores. The line scans can be better understood by separating the collected intensity

I into these two contributions, $I = I_m + \Delta I$. I_m is the minimum intensity. This is the uniform intensity that is transmitted and collected, regardless of the tip position. ΔI is the variation in the line scan above the minimum intensity. ΔI includes the structure in the line scan. Figures 4–6 show that I_m is approximately the collected intensity at the bridge site, which varies approximately as NA^2 . The uniform response of the NCG is proportional to the total phase space area of the collected light. The amplitude for variations of ΔI for a line scan along x is the difference in intensity $I_c - I_b$ between center and bridge sites. As a function of increasing NA, $I_c - I_b$ first rapidly increases, peaks, and then slowly decreases. The amplitude for variations in ΔI is a maximum for line scans collected with $\text{NA} \approx 0.3 - 0.35$ for $\lambda = 488$ nm and $\text{NA} \approx 0.4 - 0.45$ for $\lambda = 670$ nm. For both λ , the maximum amplitude for variations in a line scan occurs for collection with $\lambda/\text{NA} \approx 4r_c$, where r_c is the radius of the channel glass. The minimum wavelength λ_{min} for the in-plane variation of the light collected by the optics for a particular NA is λ/NA . The maximum amplitude for variations in a line scan occurs when the scans are collected with an NA that just accepts light concentrated in modes that can fill the channel glass core with half a wavelength (i.e., the lowest order “channel” mode with transverse wavelength $\lambda_{\text{trans}} \approx 4r_c \approx \lambda_{\text{min}}$ as one would expect if the channels were waveguides with strong confinement of the fields).

B. Importance of the tip field

Calculations have been done to determine the effect of structure in the tip field on the line scans. In the Bethe-Bouwkamp model for the aperture field, the polarization of \mathbf{E}_{ap} is determined by the polarization of the plane-wave field incident on the hole in the screen. We tried different polarizations of the incident field in the BB model and found no significant differences in the calculated line scans. This is consistent with the experimental observation that the images were insensitive to polarization. This insensitivity is another indication that the local variations in the images arise from the NCG photonic modes that are concentrated in the channel-glass cores and have cylindrical symmetry in the cores.

The effect of the separation z_{ap} , of the aperture from the NCG and of the aperture radius a on the line scans has been tested as well. Figure 7 shows the dependence on z_{ap} for $\lambda = 488$ nm and 0.7NA. Similar results were seen for other NA's and for $\lambda = 670$ nm. As the tip/sample separation increases, there is little change in the average collected intensity. There is also little change in the structure in I until the contrast reverses at large z_{ap} ($z_{\text{ap}} \approx 500$ nm). This suggests that the NCG modes that transmit light through the thick film do not couple efficiently to the strongly localized evanescent modes emitted by the tip and that the structure in the line scans is related to the mode density in the NCG rather than the field distributions near the tip. Line scans calculated by including only the propagating tip modes are almost identical to line scans calculated with both the propagating and the evanescent tip modes. This confirms the experimental observation that the evanescent tip modes did not couple effectively to the modes in the NCG that was imaged. The average collected I is insensitive to z_{ap} because the tip modes that

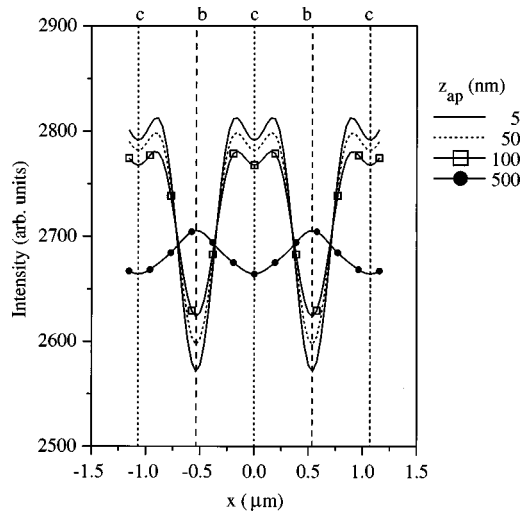


FIG. 7. Transmitted intensity line scan along x : $\lambda=488$ nm, $a=50$ nm, $NA=0.7$. Dependence on tip/sample separation z_{ap} is shown.

couple to the NCG are propagating modes that reach the NCG without any decay in intensity. When z_{ap} is small, the tip-field couples to one core at a time. The contrast reverses at large z_{ap} possibly because the coupling to multiple channels simultaneously is more efficient when the tip is between channels rather than centered on a channel. Contrast reversal at large z_{ap} was also observed experimentally.

The dependence of the line scans on tip radius a is shown in Fig. 8 at $0.7NA$ and $\lambda=488$ nm for the tip close to the NCG, i.e., $z_{ap}=10$ nm. Similar results were seen for other NA and λ . The intensity of the aperture field increases rapidly with increasing a . We eliminate this dependence by scaling the line scans to have the same average intensity. In the figure, the scans have been shifted for clarity. For small tips with $a \lesssim 100$ nm, the structure is independent of tip size. Again, this suggests that the NCG modes that transmit light through the thick film do not efficiently couple to the strongly localized tip modes. The structure persists but weakens for $100 \lesssim a \lesssim 300$ nm and the contrast reverses for a

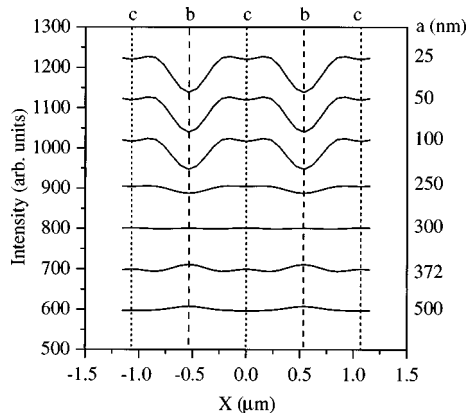


FIG. 8. Transmitted intensity line scan along x : $\lambda=488$ nm, $z_{ap}=10$ nm, $NA=0.7$. Dependence on tip radius a is shown. The line scans have been scaled to have the same average intensity (1000 on the scale used) and then shifted for clarity from the scan for $a=100$ nm by multiples of 100.

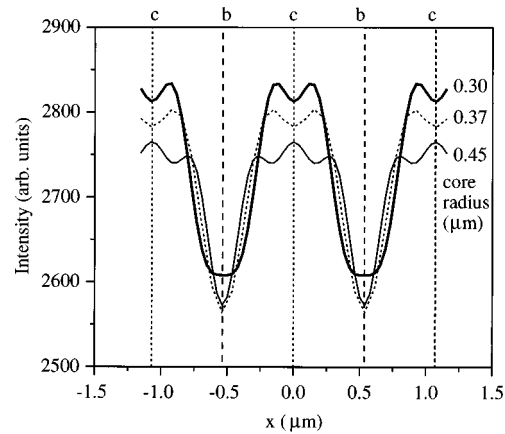


FIG. 9. Transmitted intensity line scan along x : $\lambda=488$ nm, $z_{ap}=10$ nm, $NA=0.7$, $a=50$ nm. Dependence on channel-glass core radius is shown.

≥ 300 nm. The structure weakens and reverses contrast when the tip becomes wide enough to couple to multiple channels simultaneously.

C. Significance of photonic-crystal optical modes

In this section we show that the structure in the line scans is related more closely to the density of the photonic modes in the NCG that are concentrated in the cores and not as closely to the density of the more extended, nearly uniform modes or to the structure in the tip field. We present line scans for different channel-glass sizes and different NCG lattice constants in Figs. 9 and 10. The calculations are done for $0.7NA$ and $\lambda=488$ nm for a 50 -nm tip radius. As the size of the channel glass increases, the width of the central peak in the line scan increases. The separation between the side peaks that produce the rings in the images also increases. For each core size, the ring structure occurs well inside the channel glass and does not give a direct measure of the channel-glass size. Additional structure develops as the glass core

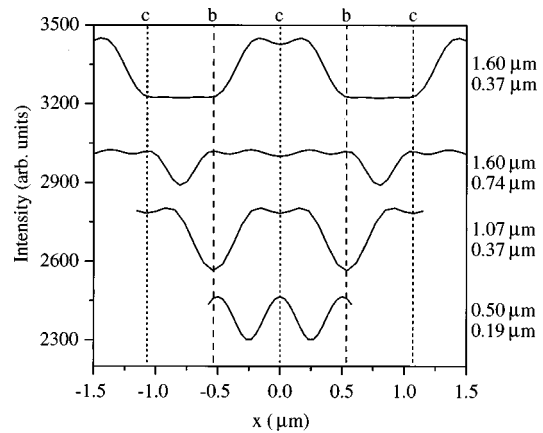


FIG. 10. Transmitted intensity line scan along x : $\lambda=488$ nm, $z_{ap}=10$ nm, $NA=0.7$, $a=50$ nm. Dependence on lattice constant and channel-glass core radius is shown. The curves are all on the same scale but have been shifted for clarity from the scan for the experimental sample (lattice constant $1.07 \mu\text{m}$ and core radius $r_c=0.37 \mu\text{m}$) by multiples of 300. The positions of the core centers (c) and bridge sites (b) for the NCG studied experimentally are indicated.

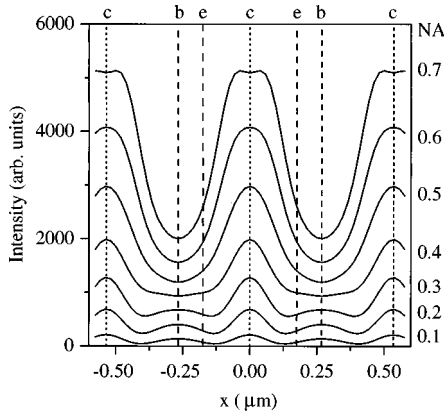


FIG. 11. Transmitted intensity line scan along x : $\lambda = 488$ nm, $z_{ap} = 10$ nm, $a = 50$ nm. Dependence on NA is shown. The NCG lattice constant is $0.535 \mu\text{m}$, the channel-glass core radius is $0.186 \mu\text{m}$, and the index contrast is $\Delta n = 1.0$. The NCG sample is $250 \mu\text{m}$ thick. The vertical lines indicate channel-glass centers (c), bridge sites (b), and edges of the channel glass (e).

increases in size and additional modes can be concentrated at the cores. The ring structure is eliminated by reducing the core size and making it difficult for any mode except the lowest-order mode to be concentrated on the cores. The line scans show a similar dropoff near the glass-core edge for different core sizes, indicating that the spread of corelike modes into the matrix glass, which depends weakly on core-glass size, determines the dropoff. The core-glass size and the lattice constant can be varied separately. Figure 10 shows that the structure in the line scans is determined by the NCG modes that are concentrated to the glass cores. Increasing the NCG lattice constant increases the spacing between the main features in the scan without changing the structure in those features.

D. High-contrast samples

The structure in the experimental images and in the line scans discussed so far results because the NCG supports photonic modes that are concentrated on the channel-glass cores. The structure is insensitive to the tip field when the tip-field only couples to one channel at a time. Contrast reversal occurs when the tip field couples to multiple channels simultaneously. Transmission of the evanescent near fields from the tip through the NCG is negligible in the samples studied for two reasons. First, the transverse wave vector k_{ev} for localized evanescent modes emitted by the tip is much larger than the reciprocal-lattice basis vectors of the NCG samples, i.e., $k_{ev} \approx \pi/(2a) \gg G_x^0, G_y^0$. The evanescent modes can couple to the NCG photonic modes in the experimental samples only through very high-order Fourier components of the index-of-refraction profile. To enhance this coupling, one can reduce the NCG lattice constant so that the tip field and the index profile vary on the same length scale in the plane, i.e., so that k_{ev} is comparable to G_x^0 and G_y^0 . One can also increase the index contrast Δn . In Fig. 11 we show line scans calculated for an NCG with half the lattice constant and half the core-glass radius of the experimental samples, with the same index for the matrix glass as in the experimental samples, but an index contrast $\Delta n = 1$ that is much bigger than in the experimental samples. The sample thickness was chosen to

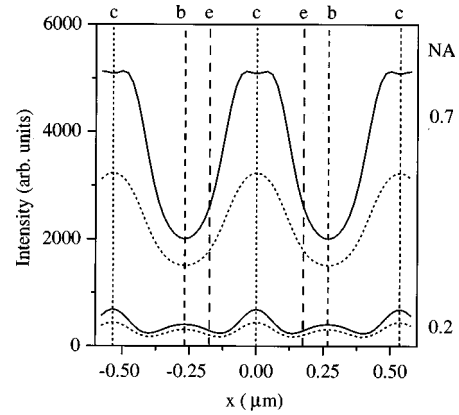


FIG. 12. Comparison of transmitted intensity line scan along x : $\lambda = 488$ nm, $a = 50$ nm, $z_{ap} = 10$ nm (—), and 50 nm (---). The NCG has the same lattice parameters, thickness, and index contrast as in Fig. 11. Dependence on NA is shown.

be $250 \mu\text{m}$ as in the experimental samples. The calculations were done as a function of NA for $\lambda = 488$ nm with a 50 -nm radius tip, scanning 10 nm from the NCG. The structure in the line scans is similar to that obtained for the experimental samples with only 1 – 2% index contrast. At low NA, a single central peak occurs. As NA increases, this peak broadens, flattens, and then evolves into the ring structure. However, the peak/bridge site contrast ratios are much larger when $\Delta n = 1$. A comparison of line scans of the high Δn sample done at $z_{ap} = 10$ nm with line scans done at $z_{ap} = 50$ nm (see Fig. 12) shows a much stronger dependence on z_{ap} than seen for low Δn samples (Fig. 7). There is a large decrease in total transmitted intensity for the same change in tip height when $\Delta n = 1$. More importantly, the structure in the line scans of the high Δn sample changes significantly as the tip height changes from 10 to 50 nm. The ring structure disappears when z_{ap} is increased from 10 to 50 nm above the high Δn sample.

These calculations were done for a 250 - μm -thick sample. Many of the NCG modes that couple to tip-evanescent fields are evanescent modes. These NCG modes make a negligible contribution to transmission through a thick sample. Transmission of evanescent fields from the tip through the sample

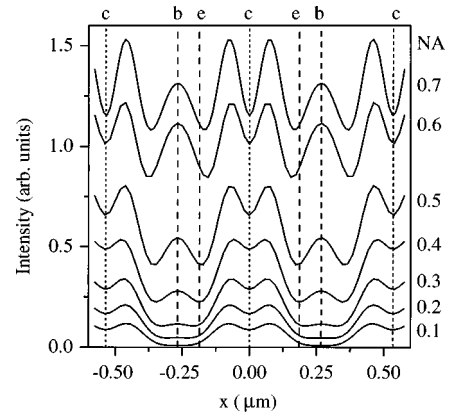


FIG. 13. Transmitted intensity line scan along x : $\lambda = 488$ nm, $z_{ap} = 10$ nm, $a = 50$ nm. Dependence on NA is shown. The NCG lattice constant is $0.535 \mu\text{m}$, the channel-glass core radius is $0.186 \mu\text{m}$, and the index contrast is $\Delta n = 1.0$. The NCG sample is $0.10 \mu\text{m}$ thick.

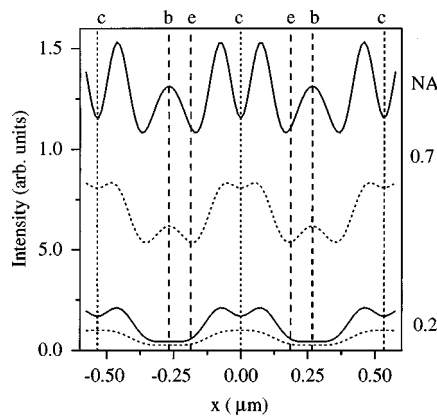


FIG. 14. Comparison of transmitted intensity line scan along x : $\lambda = 488$ nm, $a = 50$ nm, $z_{ap} = 10$ nm (—), and 50 nm (· · · · ·). The NCG has the same lattice parameters, thickness, and index contrast as in Fig. 13. Dependence on NA is shown.

can be enhanced by reducing the sample thickness. Figure 13 shows line scans done for the same sample as for Fig. 11 except that the sample thickness is only $0.1 \mu\text{m}$. Increased transmission of the evanescent tip fields by the evanescent sample modes greatly enhances the structure in the line scans. The ring structure is much more prominent. Additional structures at interstitial sites, such as the bridge sites, is now present. A comparison (Fig. 14) of the line scans for $z_{ap} = 10$ nm and $z_{ap} = 50$ nm again shows a strong z_{ap} dependence both at high and low NA. Calculations for samples that are approximately a wavelength thick show additional Fabry-Pérot structure. The thickness of the sample determines which sample modes provide enhanced transmission. The tip/sample separation determines how strongly these modes are excited.

V. CONCLUSIONS

A theory has been presented to model recent transmission NSOM images made of nanochannel-glass arrays. The theory describes the entire process of image formation, including the tip field that is the light source, the photonic modes of the nanochannel-glass array, coupling of the tip

field to the sample modes, and transmission of the fields to the collection optics. The theory is able to reproduce the key features observed in the experimental images, including the evolution of the images with increasing numerical aperture of the collection optics and the dependence on wavelength. Most importantly, the theory is able to explain a ringlike structure that develops in the images as the numerical aperture is increased.

For the samples studied experimentally, transmission NSOM probes most directly the photonic mode structure of the nanochannel-glass array. The structure in the images can be related to the photonic modes of the array that are strongly concentrated at the glass cores. The numerical aperture of the collection optics can be varied to control the size of the phase space of the photonic modes that is sampled by the transmission experiments. Angle-resolved mapping of the photonic modes could be achieved by collecting light transmitted at specific angles. The structure in the images is insensitive to the details of the tip field because the samples do not couple strongly to the localized evanescent modes emitted by the tip. In these experiments the images become sensitive to the tip field only if the tip field is so broad that it can simultaneously excite multiple channel-glass cores in the array.

Contrast and structure in the images can be enhanced greatly by increasing the transmission of the evanescent tip fields through the sample. This can be accomplished by choosing samples with higher index contrast or with index profiles with spatial variations that more closely match the spatial localization of the tip field. This enhanced contrast comes at the price of increased sensitivity to the tip field. This increased sensitivity can be exploited to better probe the sample, but it must be understood to properly separate sample properties from probe properties.

ACKNOWLEDGMENTS

We thank P. S. Julienne for helpful discussions. E.B.M. acknowledges financial support from ONR and J.W.P.H. from Sloan Research. Work done at the University of Virginia was supported by the NSF, and that at NRL was supported by DARPA and ONR.

¹D. W. Pohl, in *Advances in Optical and Electron Microscopy*, edited by C. J. R. Sheppard and T. Mulvey (Academic, London, 1991), Vol. 12, p. 243.

²*Near Field Optics*, Vol. 242 of *NATO Advanced Studies Institute, Series E: Applied Sciences*, edited by D. W. Pohl and D. Courjon (Kluwer, Dordrecht, 1993).

³D. Courjon and C. Bainier, *Rep. Prog. Phys.* **57**, 989 (1994).

⁴*Ultramicroscopy*, edited by M. Paesler and N. van Hulst (Elsevier, Amsterdam, 1995), Vol. 61, Nos. 1–4.

⁵M. A. Paesler and P. J. Moyer, *Near Field Optics: Theory, Instrumentation, and Applications* (Wiley, New York, 1996).

⁶C. Girard and A. Dereux, *Rep. Prog. Phys.* **59**, 657 (1996).

⁷E. B. McDaniel, J. W. P. Hsu, L. S. Goldner, R. J. Tonucci, E. L. Shirley, and G. W. Bryant, *Phys. Rev. B* **55**, 10 878 (1997).

⁸R. J. Tonucci, B. L. Justus, A. J. Campillo, and C. E. Ford, *Science* **258**, 783 (1992).

⁹See, for example, J. D. Joannopoulos, R. D. Meade, and J. N. Winn, *Photonic Crystals* (Princeton University Press, Princeton, 1995); or *J. Mod. Opt.* **41** (1994).

¹⁰H. A. Bethe, *Phys. Rev.* **66**, 163 (1944).

¹¹C. J. Bouwkamp, *Philips Res. Rep.* **5**, 321 (1950); **5**, 401 (1950).

¹²In free space the numerical aperture $NA = \sin(\theta)$ where θ is the half angle of the acceptance cone.

¹³D. Van Labeke, D. Barchiesi, and F. Baida, *J. Opt. Soc. Am. A* **12**, 695 (1995).

¹⁴E. Betzig and R. J. Chichester, *Science* **262**, 1422 (1993).

¹⁵A. Roberts, *J. Opt. Soc. Am. A* **4**, 1970 (1987).

¹⁶A. Roberts, *J. Appl. Phys.* **70**, 4045 (1992).

¹⁷R. D. Grober, T. Rutherford, and T. D. Harris, *Appl. Opt.* **35**, 3488 (1996).

¹⁸E. B. McDaniel and J. W. P. Hsu, *J. Appl. Phys.* **81**, 2488 (1997).